Monthly Notices of the ROYAL ASTRONOMICAL SOCIETY

MNRAS **504,** L22–L27 (2021) doi:10.1093/mnrasl/slab031
Advance Access publication 2021 March 27

TXS 1206 + 549: a new γ-ray-detected narrow-line Seyfert 1 galaxy at redshift 1.34?

Suvendu Rakshit [1,2]★ Malte Schramm,[3] C. S. Stalin [4]★ I. Tanaka,[5] Vaidehi S. Paliya [1,6] Indrani Pal [4] Jari Kotilainen[2,7] and Jaejin Shin[8]

[1]*Aryabhatta Research Institute of Observational Sciences, Manora Peak, Nainital 263002, India*
[2]*Finnish Centre for Astronomy with ESO (FINCA), University of Turku, Quantum, Vesilinnantie 5, 20014, Finland*
[3]*Graduate school of Science and Engineering, Saitama Univ. 255 Shimo-Okubo, Sakura-ku, Saitama City, Saitama 338-8570, JAPAN*
[4]*Indian Institute of Astrophysics, Block II, Koramangala, Bangalore 560034, India*
[5]*Subaru Telescope, National Astronomical Observatory of Japan, 650 North A'ohoku Place, Hilo, HI 96720,USA*
[6]*Deutsches Elektronen Synchrotron DESY, Platanenallee 6, D-15738 Zeuthen, Germany*
[7]*Tuorla Observatory, Department of Physics and Astronomy, FI-20014 University of Turku, 20014, Finland*
[8]*Department of Astronomy and Atmospheric Sciences, Kyungpook National University, Daegu 41566, Republic of Korea*

Accepted 2021 March 24. Received 2021 February 24; in original form 2020 December 8

ABSTRACT

Radio and γ-ray loud narrow-line Seyfert 1 galaxies (NLS1s) are unique objects to study the formation and evolution of relativistic jets, as they are believed to have high accretion rates and powered by low mass black holes contrary to that known for blazars. However, only about a dozen γ-ray-detected NLS1s (γ-NLS1s) are known to date and all of them are at $z \leq 1$. Here, we report the identification of a new γ-ray-emitting NLS1 TXS 1206 + 549 at $z = 1.344$. A near-infrared spectrum taken with the *Subaru Telescope* showed H β emission line with FWHM of 1194 ± 77 km s^{-1} and weak [O III] emission line but no optical Fe II lines, due to the limited wavelength coverage and poor signal-to-noise ratio. However, UV Fe II lines are present in the SDSS optical spectrum. The source is very radio-loud, unresolved, and has a flat radio spectrum. The broad-band spectral energy distribution of the source has the typical two hump structure shown by blazars and other γ-NLS1s. The source exhibits strong variability at all wavelengths such as the optical, infrared, and γ-ray bands. All these observed characteristics show that TXS 1206 + 549 is the most distant γ-NLS1 known to date.

Key words: galaxies: active – galaxies: jets – galaxies: Seyfert – gamma rays: galaxies.

1 INTRODUCTION

The physical processes required to launch powerful relativistic jets in active galactic nuclei (AGNs) are still unclear inspite of observational advances across wavelengths in the recent years. According to Laor (2000), AGNs hosted in elliptical galaxies with black hole (BH) masses $>10^8$ M$_\odot$ can produce large-scale relativistic jets while AGNs hosted in late-type galaxies with less massive BHs are mostly unable to produce relativistic jets. This suggests that massive BHs are needed to launch powerful relativistic jets. However, the detection of γ-ray emission (Abdo et al. 2009; Paliya et al. 2018) from a few radio-loud narrow-line Seyfert 1 galaxies (NLS1s) unambiguously argues for the presence of closely aligned relativistic jets in them similar to blazars (Yuan et al. 2008). This therefore challenges our understanding of how relativistic jets are formed, as NLS1s are usually powered by low-mass BHs in late-type galaxies (Olguín-Iglesias, Kotilainen & Chavushyan 2020), while blazars are believed to be powered by high-mass BHs in elliptical galaxies.

NLS1s (Osterbrock & Pogge 1985) constitute a unique class of AGNs having a low BH mass accreting close to the Eddington limit (Mineshige et al. 2000; Rakshit et al. 2017), showing strong optical Fe II emission, soft X-ray excess (Ojha et al. 2020), and lower amplitude of optical variation (Rakshit & Stalin 2017) compared to their broad-line counterparts. Although only 5 per cent NLS1s are radio loud (Komossa et al. 2006), a small number of only 16 are found to be detected in high-energy γ-rays (see Paliya et al. 2018, 2019, and references therein). It has been argued that the low BH mass of NLS1s could be due to orientation effects caused by the flat geometry of the broad-line region (BLR; e.g. Decarli et al. 2008).

The definition of NLS1 requires the full width at half-maximum (FWHM) of the H β emission line to be lesser than 2000 km s^{-1} (Osterbrock & Pogge 1985). Most of the NLS1s that we know as of today are from large optical spectroscopic surveys and are therefore at $z < 0.8$ (Williams, Pogge & Mathur 2002; Zhou et al. 2006; Rakshit et al. 2017; Chen et al. 2018). At high redshift, it is expected to detect luminous objects and hence identification of NLS1 at $z > 1$ could be crucial to verify the claims that NLS1s are low-luminosity AGN as well as to understand the nature of these sources, and how they differ from the classical Seyfert 1 galaxies. Of the NLS1s, only 16 are detected in the γ-ray band and among them only two are at redshift beyond 0.8; SDSS J1222 + 0413 at $z = 0.966$ (Yao et al. 2015) and SDSS J094635.06 + 101706.1 at $z = 1.004$ (Yao et al. 2019). Here, we report the identification of a γ-ray-detected NLS1

★ E-mail: suvenduat@gmail.com (SR); stalin@iiap.res.in (CSS)

TXS 1206 + 549 (SDSS J120854.24 + 544158.1) at $z = 1.344$. This is based on the infrared spectroscopic observations carried out using the 8.2 m *Subaru Telescope* that showed the presence of H β line with FWHM of 1194 ± 77 km s^{-1} and [O III] to H β flux ratio ∼0.7. The optical Fe II lines are not seen in the Subaru spectrum; however, UV Fe II lines are present in the optical spectrum from the Sloan Digital Sky Survey (SDSS; see Section 2). The multiband properties of this source are presented in Section 3 with a discussion and conclusion in Section 4. Throughout the paper, a cosmology with $H_0 = 70$ km s^{-1} Mpc^{-1}, $\Omega_\Lambda = 0.7$, and $\Omega_M = 0.3$ is assumed.

2 SPECTROSCOPY

2.1 Optical

To find high-z γ-ray-emitting NLS1s, we cross-matched the fourth catalogue of AGNs detected by the Fermi/LAT (4LAC; Ajello et al. 2020) with the spectral catalogue of SDSS DR14 quasars (Rakshit, Stalin & Kotilainen 2020) that provides spectral properties of around 500 000 quasars. We looked for potential narrow Mg II line objects with FWHM < 2500 km s^{-1} and showing traces of strong Fe II complex and identified a NLS1 candidate, TXS 1206 + 549, at $z = 1.344$ with FWHM (Mg II) $= 2419 \pm 581$ km s^{-1}. The redshifted H β line falls outside of the SDSS spectral coverage, and thereby preventing a secure NLS1 classification of the source.

Looking into the SDSS archive, we found three optical spectra of TXS 1206 + 549. Since Mg II doublets are clearly resolved, we carefully modeled all the three spectra. First, we fit the 2200−3500 Å AGN continuum using a combination of power-law, a Balmer pseudo-continuum (Grandi 1982), and the Fe II template from Tsuzuki et al. (2006) as described in Shin et al. (2019). After fitting and subtracting the continuum, each of the Mg II λλ2796, 2803 doublet lines were fitted with a broad and narrow components following Wang et al. (2009). The broad components were modeled with either a Gaussian or a Lorentzian. The width and velocity of the doublets were tied and the flux ratio was varied between 2:1 and 1:1. The narrow components were modeled using single Gaussian with same constrains as above. The decomposition of the SDSS spectrum for the epoch MJD = 57430 is shown in the left-hand panel of Fig. 1. The best-fitting spectral properties are summarized in Table 1. The FWHM (Mg II) is found to be between 2000 and 3000 km s^{-1} depending on the model used to represent the broad Mg II doublets and the epoch used. Broad-line profile was similarly well fitted with either a Gaussian or a Lorentzian profile; however, in the latter case, a lower FWHM of Mg II lines was found hinting the NLS1 nature of TXS 1206 + 549. To confirm this, we carried out Subaru near-infrared (IR) spectroscopy to detect and characterize the redshifted H β line.

2.2 Near-infrared

Subaru/MOIRCS long-slit near-infrared (NIR) spectroscopic observations were obtained on 2020 July 20, as part of performance verification observations for the new LightSmyth J-band Grism (Tanaka et al. in preparation). Weather condition was good, with ∼0.8 arcsec seeing. We chose the 0.8 arcsec-width slit, by which we got a spectral resolution of R∼2200. The exposure time was 300 s with 12-times multisampling, and a standard A-B dither (4 arcsec throw length) was applied. In total three sequences were observed with a total integration time of 1800 s. The data was reduced following standard reduction procedures for long-slit spectroscopy using IRAF.[1] The spectrum was smoothed by a 5-pixel box-car to increase the S/N and then brought to the rest-frame.

The Subaru spectrum, covering the rest-frame wavelength range of 4778−5247 Å is shown in the right-hand panel of Fig. 1. To estimate the emission line parameters, we fit the spectrum using a power-law continuum, a single Gaussian for H β line and a double Gaussian for each of the [O III]λ5007 and [O III]λ4959 doublets. Since no narrow component is clearly visible in the H β line, we did not attempt to decompose it. Furthermore, due to insufficient wavelength coverage below 4700 Å, the decomposition of optical Fe II was not performed. The decomposed model components are shown in Fig. 1 and the best-fitting emission line parameters are given in Table 1. The FWHM of H β is 1194 ± 77 km s^{-1} and the flux ratio of [O III]λ5007 to H β is ∼0.7, satisfying the criteria of a NLS1. We note significant UV Fe II emission in the SDSS spectrum but the insufficient wavelength coverage of the near-IR spectrum prevents us to discuss its optical Fe II strength.

3 MULTIBAND PROPERTIES

3.1 Radio-band

TXS 1206 + 549 is detected in many radio surveys. It appears to be a point source in the radio image of VLBA Imaging and Polarimetry Survey (VIPS; Helmboldt et al. 2007) at 5 GHz with a peak (θ_{peak}) and integrated (θ_{int}) flux densities of 231.6 and 264.5 mJy ($L_{int} = 1.2 \times 10^{34}$ erg s^{-1} Hz^{-1}), respectively, displaying powerful Fanaroff–Riley (FR) type II radio jets. The concentration parameter $\theta = \sqrt{\theta_{int}/\theta_{peak}}$ (Ivezić et al. 2002) is 1.07 close to 1.06 for the source to be 'resolved' according to Kimball & Ivezić (2008), indicating compact structure. Such compact and powerful radio jets of TXS 1206 + 549 indicate similarities with blazars.

The spectral index is flat with $\alpha_r = 0.3$ between 1.4 and 4.85 GHz ($s_\nu \propto \nu^{\alpha_r}$; White & Becker 1992) and $\alpha_r = 0.23$ between 147 MHz (TIFR GMRT Sky Survey) and 1.4 GHz (NRAO/VLA Sky Survey; de Gasperin, Intema & Frail 2018). The source is known to be highly variable in the radio, with the radio flux varying between 160 and 302 mJy at 1.4 GHz within a time-scale of few years. Liodakis et al. (2018) modeled the 15 GHz light curve of this source observed by the Owens Valley Radio Observatory (OVRO) as a combination of multiple flares and estimated brightness temperature $T_{var} = 5 \times 10^{14}$ K, Doppler factor $\delta_{var} = 29.09^{+10.28}_{-10.02}$ indicating high Doppler-boosted emission. We estimated the radio loudness (R) of this source using $R = f_\nu(5\ \mathrm{GHz})/f_\nu(4400\ \text{Å})$, where $f_\nu(5\ \mathrm{GHz}) = 252$ mJy at VLA 5 GHz (Linford et al. 2012) and $f_\nu(4400\ \text{Å})$ is taken from Rakshit et al. (2020). The source is very radio loud with $R \sim 1300$. However, the radio loudness can have a large range due to high amplitude of variation seen in the optical (∼2 magnitude; see next section) and radio bands (a factor of 2).

3.2 Infrared and optical variability

We collected infrared photometry of TXS 1206 + 549 observed by the *Wide-field Infrared Survey Explorer* (WISE; Wright et al. 2010) from ALLWISE and NEOWISE database (Mainzer et al. 2014). The WISE 3.4 μm (W1) and 4.6 μm (W2) band light curves are shown in the top panel of Fig. 2. We calculated the intrinsic variability amplitude σ_m (Rakshit et al. 2019) i.e. the variance of the observed light curve after removing the measurement uncertainty. The duty

[1] Image Reduction and Analysis Facility.

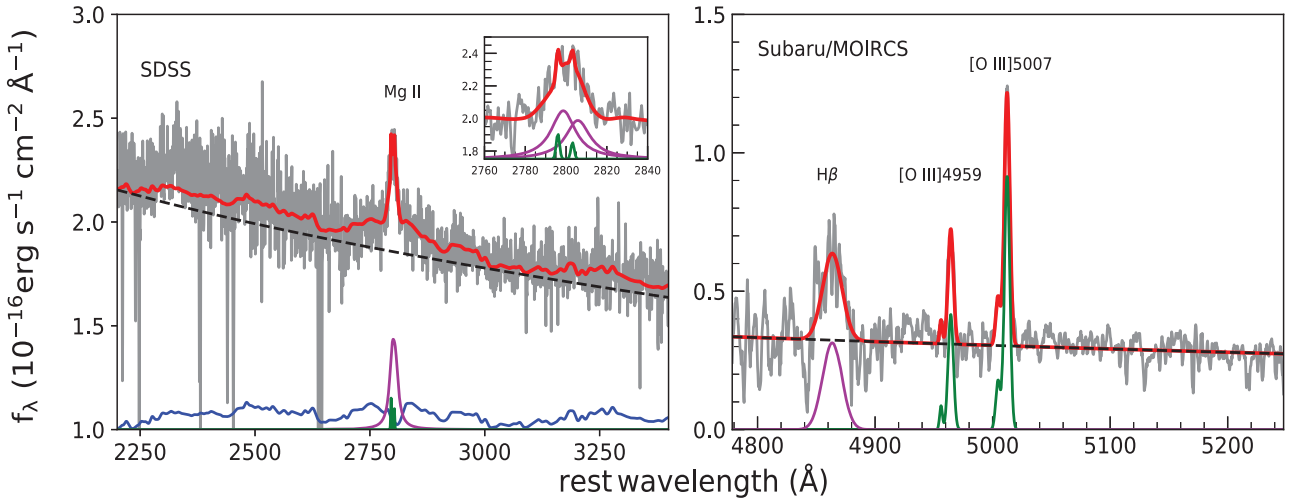

Figure 1. Spectrum of TXS 1206 + 549. Left: Mg II line fit of the SDSS spectrum for MJD = 57430. The data (grey), best-fitting model (red) and power-law plus Balmer continuum (black dashed) are shown along with the decomposed broad (magenta) and narrow (green) components of Mg II, and Fe II in UV (blue). The inset plot shows the zoomed version of Mg II line fitting. Right: H β model fit to the Subaru spectrum. The data (grey), best-fitting model (red), power-law continuum (black dashed), decomposed broad line (magenta) and narrow lines (green) are shown.

Table 1. Spectral properties of TXS 1206 + 549. Line widths are not corrected for instrumental resolution. The luminosity of UV Fe II in the wavelength range of 2200−3090 Å is also given. Due to poor signal-to-noise ratio (S/N), [O II] λ3727 emission line parameters for spectrum at MJD = 52672 are not calculated.

SDSS ID	model (Mg II, br)	FWHM (Mg II, br) (km s^{-1})	EW (Mg II, br) (Å)	SDSS spectra Flux (Mg II, br) (erg s^{-1} cm^{-2})	Flux (Fe II, UV) (erg s^{-1} cm^{-2})	L_{3000} (erg s^{-1})	FWHM ([O II]λ3727) (km s^{-1})	Flux ([O II]λ3727) (erg s^{-1} cm^{-2})
1018-52672-0120	Gaussian	2975 ± 261	18.7 ± 1.1	133.59 ± 8.11	604.33 ± 59.25	45.295 ± 0.004	–	–
	Lorentzian	2560 ± 270	22.1 ± 1.9	158.64 ± 14.05	501.99 ± 66.40	–	–	–
6688-56412-0776	Gaussian	2838 ± 220	12.0 ± 0.9	100.99 ± 7.79	652.82 ± 45.19	45.370 ± 0.002	662 ± 158	23.29 ± 4.14
	Lorentzian	2353 ± 161	14.5 ± 0.8	122.33 ± 6.70	593.31 ± 40.70	–	–	–
8229-57430-0099	Gaussian	2838 ± 370	5.2 ± 0.6	96.62 ± 12.17	666.09 ± 56.32	45.718 ± 0.001	584 ± 71	27.18 ± 2.82
	Lorentzian	2076 ± 280	6.3 ± 0.6	117.22 ± 12.16	619.98 ± 54.49	–	–	–
				Subaru spectrum				
		log L_{5100} (erg s^{-1})	Model (H β)	FWHM (H β) (km s^{-1})	Flux (H β) (erg s^{-1} cm^{-2})	Flux ([O III]λ5007) (erg s^{-1} cm^{-2})		
		45.20 ± 0.05	Single Gaussian	1194 ± 77	76.65 ± 1.03	51.96 ± 0.55		

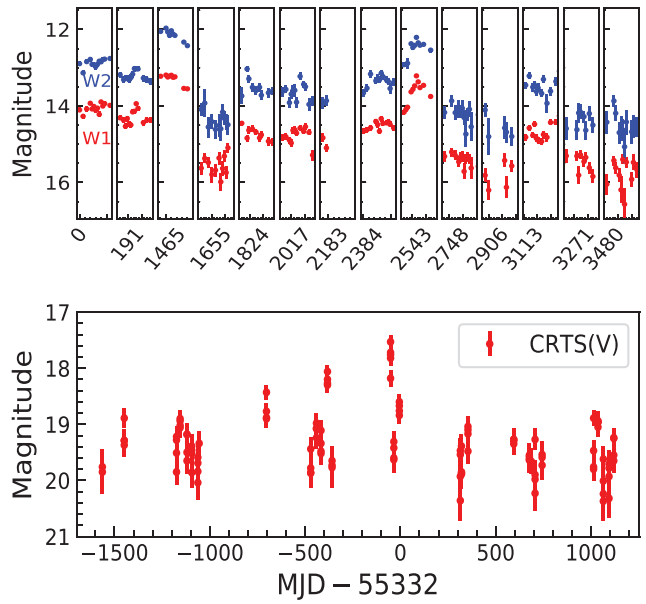

Figure 2. Top: WISE light curve of TXS 1206 + 549 in 3.4 μm (W1) and 4.6 μm (W2) bands with each box representing a duration of 1.2 d. Bottom: Optical photometric light curve from CRTS (*V*-band).

cycle (Romero, Cellone & Combi 1999), which is the fraction of time when an object is variable on intra-day (i.e. 1.2 d) time-scale (see also Rakshit et al. 2019) was found to be 91 per cent and 79 per cent in W1 and W2 bands, respectively, suggesting that TXS 1206 + 549 is highly variable. The maximum variation was found on 2 May 2017 with $\sigma_m = 0.65 \pm 0.10$ mag in W1 and 0.68 ± 0.11 mag in W2 bands. Observations of such short time-scale variations in the IR indicate that the emission region is compact, much smaller than the dust torus, and the emission is dominated by non-thermal emission from the jet (see Jiang et al. 2012; Rakshit et al. 2019). In the 10 yr of WISE observations, TXS 1206 + 549 showed large amplitude variation with $\sigma_m = 0.73 \pm 0.04$ mag in W1 and 0.69 ± 0.04 mag in W2 bands. This is similar to the variation of other γ-ray-detected NLS1s (γ-NLS1s; Rakshit et al. 2019).

We also looked for archival optical photometry of TXS 1206 + 549. The optical light curve using data acquired by the Catalina Real-Time Transient Survey (CRTS; Drake et al. 2009) is shown in the bottom panel of Fig. 2. Large amplitude flux variation with $\sigma_m = 0.52 \pm 0.04$ mag is found in the optical over the 7 yr of CRTS observations. This too is consistent with the high amplitude optical variation observed in other γ-ray-detected radio-loud NLS1s (Rakshit & Stalin 2017; Yao et al. 2019).

3.3 X-ray and γ-ray emission

TXS 1206 + 549 was observed by *SWIFT−XRT* (Burrows et al. 2005) six times between 2011 March and 2018 February. Among them, only the OBSID 00040572002 has sufficient S/N for spectral analysis. For this OBSID, we generated the spectrum using the online version of the *SWIFT−XRT* data products generator.[2] Fitting the spectrum with the model TBabs∗zTBabs∗powerlaw we obtained a photon index of $1.7^{+0.7}_{-0.4}$ that is relatively flat compared to the radio-quiet NLS1s but similar to the γ-NLS1s (Paliya et al. 2019). The flux in the 0.3−10 keV band is $7.0^{+2.8}_{-2.4} \times 10^{-13}$ erg s^{-1} cm^{-2} corresponding to an apparent luminosity of $\sim 1.9 \times 10^{45}$ erg s^{-1}.

TXS 1206 + 549 is detected at a significance level of 48σ and associated with the γ-ray source 4FGL J1208.9 + 5441 in the 4LAC catalogue (Ajello et al. 2020). The γ-ray flux is 1.8×10^{-11} erg s^{-1} cm^{-2} in the energy range of 100 MeV to 100 GeV and corresponds to an isotropic γ-ray luminosity of 4.8×10^{46} erg s^{-1}. The spectrum is best fitted by a log Parabola model with index $\alpha = 2.51 \pm 0.03$ and curvature $\beta = 0.07 \pm 0.02$ compared to a power-law model ($\alpha = 2.59 \pm 0.02$). The best-fitting photon index is in the range of 2.2−2.8 which is similar to that seen in other γ-NLS1s (e.g. Abdo et al. 2009; Yao et al. 2015, 2019). TXS 1206 + 549 is also variable in the γ-ray band with a fractional variability amplitude of 0.49 ± 0.12 (see Ajello et al. 2020).

3.4 Broad-band spectral energy distribution

We collected non-simultaneous, archival observations of TXS 1206 + 549 from the Space Science Data Center (SSDC[3]) and plotted the multiwavelength spectral energy distribution (SED) in Fig. 3. As can be seen, the broad-band SED of TXS 1206 + 549 exhibits the typical double hump structure similar to blazars. Indeed, this object is classified as a flat spectrum radio quasar (FSRQ) in the 4LAC catalogue (see also Tan et al. 2020).

To investigate the physical properties of the source, we reproduced the SED with the conventional synchrotron inverse Compton radiative model (see details in Dermer et al. 2009; Ghisellini & Tavecchio 2009). The associated results are plotted in Fig. 3 and the derived parameters are provided in Table 2. For the modelling, we used the geometric mean of the black hole masses computed from the H β and Mg II emission lines (see next section). The BLR luminosity ($L_{\rm BLR}$), on the other hand, was estimated from the line luminosities derived from the spectral fitting and assuming the line-scaling factors reported in Francis et al. (1991) and Celotti, Padovani & Ghisellini (1997). Assuming a 10 per cent BLR-covering factor, we calculated the accretion disk luminosity from $L_{\rm BLR}$.

The high-frequency radio to optical-UV spectrum is found to be well explained by synchrotron emission with a minor contribution from the accretion disk. The X- and γ-ray spectra are reproduced by a combination of the SSC and EC processes. This suggests a similarity of the physical properties of TXS 1206 + 549 with FSRQ type blazars. Furthermore, the derived SED parameters (Table 2) are consistent with that typically determined for broad-line blazars detected with the *Fermi*-LAT (Paliya et al. 2017).

4 DISCUSSION AND CONCLUSION

Using near-IR spectroscopy, we observed redshifted H β emission line of TXS 1206 + 549 and obtained H β FWHM of 1194 ± 77 km s^{-1} and the flux ratio of [O III]5007 to H β is low (∼0.7), suggesting TXS 1206 + 549 to be a NLS1. However, our spectrum of low S/N and limited wavelength coverage shows weak/no optical Fe II emission in TXS 1206 + 549. However, UV Fe II lines are seen in the SDSS optical spectrum. In terms of optical properties, it shows similarities with the γ-NLS1 PKS 2004 − 447 (Oshlack, Webster & Whiting 2001) having weak Fe II emission rather than the other γ-NLS1 1H 0324 + 3410 (Zhou et al. 2007) having strong Fe II emission although both of them have similar H β FWHM (∼1600 km s^{-1}). However, PKS 2004−447 exhibits a steep radio spectrum compared to the flat radio spectrum seen in TXS 1206 + 549 and 1H 0324 + 3410. We note that high S/N spectroscopic observations with a wider wavelength coverage will be helpful to quantify its optical Fe II strength and obtain detailed information about the shape of the H β profile as the broad component of NLS1s

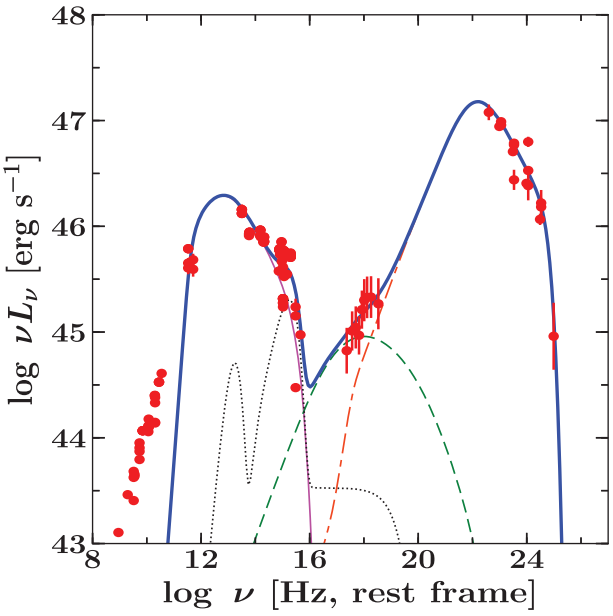

Figure 3. Rest-frame multiwavelength SED of TXS 1206 + 549 along with the results of the leptonic radiative modelling. Pink thin solid, green dashed, and orange dash–dash–dotted lines represent synchrotron, synchrotron self Compton (SSC), and external Compton (EC) processes, respectively. Thermal emission from the dusty torus, accretion disk, and corona is shown with the black dotted line. Blue thick solid line refers to the sum of all the radiative components.

Table 2. Summary of the parameters used/derived from the modelling of the SED.

Parameter	Value
Slope of the broken power law before break energy	1.6
Slope of the broken power law after break energy	4.0
Minimum Lorentz factor	1
Break Lorentz factor	206
Maximum Lorentz factor	4200
Magnetic field, in Gauss	3.2
Bulk Lorentz factor	11
Compton dominance	8
Distance of the emission region, in parsec	0.05
Size of the BLR, in parsec	0.05
Log scale black hole mass, in solar mass unit	8.07
Log scale accretion disk luminosity, in erg s^{-1}	45.39

[2] https://www.swift.ac.uk/user objects/
[3] https://tools.ssdc.asi.it/SED/

are usually better represented by a Lorentzian profile rather than a Gaussian (e.g. Véron-Cetty, Véron & Gonçalves 2001; Rakshit et al. 2017).

Using $\log L_{5100} = 45.20$ erg s^{-1} estimated from the power-law continuum and the Hβ scaling relation of Vestergaard & Peterson (2006), we obtained $M_{\rm BH} = 4.63 \times 10^7$ M$_\odot$ for TXS 1206 + 549. On the other hand, using Mg II line (Table 1) we obtained $M_{\rm BH} = 2.97 \times 10^8$ M$_\odot$ (Rakshit et al. 2020). However, black hole mass estimation based on continuum luminosity is likely to be uncertain, due to the non-thermal emission from the jet that contributes to the observed continuum flux (e.g. Rakshit 2020). The Mg II line equivalent width for TXS 1206 + 549 decreases by a factor of 3 between MJD = 52672 and 57430 (see Table 1) as the Mg II flux remains almost unchanged while continuum luminosity at 3000 Å increases by 0.4 dex suggesting significant non-thermal contribution to the continuum that does not contribute in ionizing the line-emitting gas. Therefore, we also estimated the 5100 Å continuum luminosity from the luminosity of the Hβ using the scaling relation given by Rakshit et al. (2020) and obtained $\log L_{5100} = 44.77$ erg s^{-1} and a virial black hole mass of $M_{\rm BH} = 2.8 \times 10^7$ M$_\odot$. Overall, the black hole mass of TXS 1206 + 549 is consistent with the average black hole mass of NLS1s ($<\log M_{\rm BH}> = 6.9 \pm 0.4$ M$_\odot$; Rakshit et al. 2017) and within the range of black hole mass of γ-NLS1s ($<\log M_{\rm BH}> = 7.8 \pm 0.6$ M$_\odot$) but lower than that of blazars ($<\log M_{\rm BH}> = 8.9 \pm 0.5$ M$_\odot$; Paliya et al. 2019). With a bolometric correction factor of 9.26 (Richards et al. 2006), the Eddington ratio is found to be 1.5 (using $\log L_{5100} = 44.77$ erg s^{-1}), suggesting super Eddington accretion.

TXS 1206 + 549 is a radio-loud source showing a compact radio emission. The high amplitude of infrared variability in time-scale of months to days suggests emission region is compact and significant non-thermal contribution from jet in the infrared. The SED shows a double hump structure typical for γ-ray-emitting blazars (see Fig. 3). From our model fits (see Table 2) we found magnetic field strength and bulk Lorentz factor of 3.2 Gauss and 11, respectively, similar to that found by Tan et al. (2020). The magnetic field found for TXS 1206 + 549 is similar to that of other γ-ray-emitting NLS1s (Paliya et al. 2019).

NLS1s are usually considered to be low-luminous AGN ($\log L_{\rm bol} < 46$ erg s^{-1}). However, with the discovery of more number of γ-NLS1s at high-z and higher luminosity such as TXS 1206 + 549, they smoothly join the FSRQ branch of blazars. Identification of more such high-z NLS1 and their broad-band SED analysis will allow us to have a direct comparison of the physical properties of high-$z\gamma$-NLS1s with that of high-z blazars. Such a study will allow one to probe the formation and evolution of radio jets in NLS1s (sources with low black hole mass and high accretion rate relative to Eddington) *vis-a-vis* powerful blazars (sources with high black hole mass and low accretion rate relative to Eddington).

ACKNOWLEDGEMENTS

We are thankful for the comments and suggestions by the anonymous referee that helped us to improve the manuscript. This work is based on data collected at the *Subaru Telescope* that is operated by the National Astronomical Observatory of Japan (NAOJ). Part of this work is based on archival data, software, or online services provided by the Space Science Data Center (SSDC). This work was supported by JSPS KAKENHI Grant Number JP18H03717. JK acknowledges financial support from the Academy of Finland, grant 311438. JS was supported by Basic Science Research Program through the National Research Foundation of Korea (NRF) funded by the Ministry of Education (2019R1A6A3A01093189). SR thanks Neha Sharma for carefully reading the manuscript.

DATA AVAILABILITY

The data underlying this article will be shared on reasonable request to the corresponding author.

REFERENCES

Abdo A. A., et al., 2009, ApJ, 707, L142
Ajello M., et al., 2020, ApJ, 892, 105
Burrows D. N., et al., 2005, Space Sci. Rev., 120, 165
Celotti A., Padovani P., Ghisellini G., 1997, MNRAS, 286, 415
Chen S., et al., 2018, A&A, 615, A167
de Gasperin F., Intema H. T., Frail D. A., 2018, MNRAS, 474, 5008
Decarli R., Dotti M., Fontana M., Haardt F., 2008, MNRAS, 386, L15
Dermer C. D., Finke J. D., Krug H., Böttcher M., 2009, ApJ, 692, 32
Drake A. J., et al., 2009, ApJ, 696, 870
Francis P. J., Hewett P. C. , Foltz C. B., Chaffee F. H., Weymann R. J., Morris S. L., 1991, ApJ, 373, 465
Ghisellini G., Tavecchio F., 2009, MNRAS, 397, 985
Grandi S. A., 1982, ApJ, 255, 25
Helmboldt J. F., et al., 2007, ApJ, 658, 203
Ivezić Ž., et al., 2002, AJ, 124, 2364
Jiang N., et al., 2012, ApJ, 759, L31
Kimball A. E., Ivezić Ž., 2008, AJ, 136, 684
Komossa S., Voges W., Xu D., Mathur S., Adorf H., Lemson G., Duschl W. J., Grupe D., 2006, AJ, 132, 531
Laor A., 2000, ApJ, 543, L111
Linford J. D., Taylor G. B., Romani R. W., Helmboldt J. F., Readhead A. C. S., Reeves R., Richards J. L., 2012, ApJ, 744, 177
Liodakis I., Hovatta T., Huppenkothen D., Kiehlmann S., Max-Moerbeck W., Readhead A. C. S., 2018, ApJ, 866, 137
Mainzer A., et al., 2014, ApJ, 792, 30
Mineshige S., Kawaguchi T., Takeuchi M., Hayashida K., 2000, PASJ, 52, 499
Mooney S., et al., 2019, A&A, 622, A14
Ojha V., Chand H., Dewangan G. C., Rakshit S., 2020, ApJ, 896, 95
Olguín-Iglesias A., Kotilainen J., Chavushyan V., 2020, MNRAS, 492, 1450
Oshlack A. Y. K. N., Webster R. L., Whiting M. T., 2001, ApJ, 558, 578
Osterbrock D. E., Pogge R. W., 1985, ApJ, 297, 166
Paliya V. S., Marcotulli L., Ajello M., Joshi M., Sahayanathan S., Rao A. R., Hartmann D., 2017, ApJ, 851, 33
Paliya V. S., Ajello M., Rakshit S., Mandal A. K., Stalin C. S., Kaur A., Hartmann D., 2018, ApJ, 853, L2
Paliya V. S., Parker M. L., Jiang J., Fabian A. C., Brenneman L., Ajello M., Hartmann D., 2019, ApJ, 872, 169
Rakshit S., 2020, A&A, 642, 59
Rakshit S., Stalin C. S., 2017, ApJ, 842, 96
Rakshit S., Stalin C. S., Chand H., Zhang X.-G., 2017, ApJS, 229, 39
Rakshit S., Johnson A., Stalin C. S., Gand hi P., Hoenig S., 2019, MNRAS, 483, 2362
Rakshit S., Stalin C. S., Kotilainen J., 2020, ApJS, 249, 17
Richards G. T., et al., 2006, ApJS, 166, 470
Romero G. E., Cellone S. A., Combi J. A., 1999, A&AS, 135, 477
Shin J., Nagao T., Woo J.-H., Le H. A. N., 2019, ApJ, 874, 22
Tan C., Xue R., Du L.-M., Xi S.-Q., Wang Z.-R., Xie Z.-H., 2020, ApJS, 248, 27
Tsuzuki Y., Kawara K., Yoshii Y., Oyabu S., Tanabé T., Matsuoka Y., 2006, ApJ, 650, 57
Véron-Cetty M.-P., Véron P., Gonçalves A. C., 2001, A&A, 372, 730
Vestergaard M., Peterson B. M., 2006, ApJ, 641, 689
Wang J.-G., et al., 2009, ApJ, 707, 1334
White R. L., Becker R. H., 1992, ApJS, 79, 331
Williams R. J., Pogge R. W., Mathur S., 2002, AJ, 124, 3042
Wright E. L., et al., 2010, AJ, 140, 1868

Yao S., Yuan W., Zhou H., Komossa S., Zhang J., Qiao E., Liu B., 2015, MNRAS, 454, L16
Yao S., Komossa S., Liu W.-J., Yi W., Yuan W., Zhou H., Wu X.-B., 2019, MNRAS, 487, L40
Yuan W., Zhou H. Y., Komossa S., Dong X. B., Wang T. G., Lu H. L., Bai J. M., 2008, ApJ, 685, 801
Zhou H., Wang T., Yuan W., Lu H., Dong X., Wang J., Lu Y., 2006, ApJS, 166, 128
Zhou H., et al., 2007, ApJ, 658, L13

This paper has been typeset from a TEX/LATEX file prepared by the author.